Parasitic effects of load introduction points in full-scale composite tidal turbine blade tests

DOI: 10.1784/ndt2023.3a4

Parasitic effects of load introduction points in full-scale composite tidal turbine blade tests

Miguel A Valdivia Camacho, Marek J Munko, Fergus Cuthill, Conchúr M Ó Bradaigh, Edward D McCarthy, Sergio Lopez Dubon
School of Engineering, The University of Edinburgh, The King's Buildings
Edinburgh, EH9 3JL, UK
MA.Valdivia@ed.ac.uk

Abstract
There has been a significant increase in the development of tidal energy to enhance its competitiveness compared to other renewable sources. This growth requires dedicated fatigue testing facilities for composite tidal turbine blades. In the first decades of the tidal industry, blade load introduction methods from the wind energy sector were adopted for onshore testing. However, the relevant wind energy standards determine an unsuitable area up to one blade chord length on both sides of the blade load introduction zone from stress data analysis. This study focuses on investigating the impact of concentrated forces applied to the surface of a composite blade, particularly examining its behaviour in the inter-saddle zones. To study this effect, a full-scale composite tidal blade was tested at FastBlade using actuators. During the test, multiple measuring devices and Digital Image Correlation were employed to analyse the structural response of the blade while one of the three saddles was clamped. The clamping pressure was mapped on the blade's surface, revealing a smaller disturbed area that could reduce the number of tests required to analyse the entire blade. This disturbed area is found to vary not only as a function of the chord length, but also the blade geometry and the saddle system parameters.

1. Introduction

1.1 Tidal Energy

A diverse range of green technologies is essential for ensuring energy security while meeting the electricity demand. Among these technologies, tidal energy has been regarded as a valuable addition to the UK's energy mix. Its predictability and reliability surpass those of wind and solar energy sources. The UK is surrounded by a significant tidal energy potential, estimated at 50 TWh/year, accounting for 48% of the total European resource[(1)]. If harnessed, this source of energy could contribute up to 16% of the UK's electricity consumption. However, the annual energy production from tidal sources in the UK has fluctuated over the years, reaching its peak at 14 GWh in 2019 but declining to 4 GWh in 2021[(2)]. Tidal stream turbines (TST) have proven to be effective in harnessing the kinetic energy from tides. Since the early 2000s, several field and onshore testing facilities have been established to mitigate the risks associated with the composite TST blades, which play a crucial role in the overall turbine performance.

FastBlade, as an onshore testing facility, stands out as the first full-scale regenerative tidal blade fatigue test facility. This achievement is attributed to its Digital Displacement® hydraulic system, allowing energy recovery between loading cycles at high flow rates without compromising the quality, control, or certification of tidal blades[(3)].

1.2 Load Introduction Methods

The current design and test methodology employed for tidal stream turbine (TST) blades have been adapted from the wind energy industry. In the wind sector, various load introduction configurations, such as cranes, winches, whiffle trees, and hydraulic actuators, are widely used for full-scale testing[4–6]. These systems are often equipped with a load distributor to reduce stress concentrations, with the saddle system being the most common one used. Saddles can adapt to blades of various sizes and shapes, ensuring versatility during testing. At FastBlade, the load introduction method used involves a saddle configuration composed of a combination of wood-like material and a steel frame. This design incorporates the strength of steel with the stability and flexibility of wood. The steel frame, constructed using beams or C and U-section channels, forms the main structure of the saddle. It is firmly clamped with steel rods at both ends and connected to the hydraulic actuator, providing the necessary support for the testing process. On the other hand, the wooden cradle is responsible for supporting the blade during testing. Medium-density fibreboard (MDF) is a popular choice for the wooden cradle due to its lightweight nature, natural shock absorption properties, and ease of customisation.

However, despite extensive research on test validation, the focus has primarily been on improving test accuracy rather than considering the real moment distribution along the blade, which has resulted in cases where failure occurs within the area surrounding the load introduction points[7]. This oversight resulted in very constrained testing conditions, as TST blades face more challenging conditions underwater. Shorter spans reduce the number of load introduction points per test, which in turn increases the number of tests needed to analyse the entire blade structure. Consequently, the current TST blade certification standards, like DNVGL-ST-0164[8], often reference other standards meant for wind turbine blades, leading to a lack of optimisation in evaluating TST blades. Another issue arises from the use of the blade's chord length as a reference for identifying the disturbed area on each side of the load introduction point, where the blade cannot be properly evaluated. As the chord-to-span ratio is relatively high in tidal blades compared to wind blades, adhering to the chord length criterion can leave the test with insufficient usable area along the blade for analysis.

1.3 Tidal Blade Testing Standards

At FastBlade and other test rig facilities, the test procedures adhere to international standards, enabling the certification of new blade designs before proceeding to mass-scale manufacturing. These testing standards are formulated based on extreme design load cases for static testing, while fatigue testing is conducted to validate the blades' life expectancy. For tidal energy developments, various standards and guidelines exist; however, the most widely used standard for tidal turbines is DNVGL-ST-0164[8]. This standard refers to several other service specifications and standards covering the complete manufacturing, assembly, and placement of the turbine structure, as shown in Table 1.

Amongst the previous standards, only the IEC TS 62600-2 and the IEC 61400-23 provide guidelines for load introduction points, specifying a disturbed area that cannot be used for evaluation. This disturbed area can extend up to three-quarters of a chord length or up to one chord length on either side of the fixture. However, these standards do not offer

further details on the loading structure or practices to mitigate undesired effects during testing. Due to the lack of specific guidance, the aim of this research is to understand and optimise the induced effects of load introduction points in full-scale composite TST blade tests. Strain gauges and digital image correlation (DIC) will be employed to aid in this investigation. While some studies have explored onshore testing with multiple load introduction points for full-scale tidal blade tests, they mainly focused on other aspects of the testing process. To the authors' knowledge, no studies have delved into the intricacies of saddles in a TST blade, which could minimise the impact of using multiple saddles to represent the real moment distribution more accurately along the blade.

Table 1. Relevant standards for tidal turbine design, manufacturing, and testing

Standard	Description
DNVGL-ST-0164	Main current standard for tidal turbines
IEC TS 62600-2	Design requirements
IEC TS 62600-3	Measurement of mechanical loads
DS 5760, Part 5	Guide to failure modes, effects, and criticality analysis
DNV-OS-C501	Composite components
DNVGL-ST-0376	Rotor blades for wind turbines
IEC 61400-23	Load introduction guidelines

2. Materials and Methods

2.1 Blade Specimen

The composite blade was deployed in the DeepGen IV tidal project and was a collaborative effort between Tidal Generation Limited (TGL) and Aviation Enterprises Limited for its design and manufacturing. Unfortunately, due to the dissolution of the design company, detailed technical information about the blade is limited. The tidal turbine, depicted in Figure 1a, had a capacity of 500 kW and was successfully installed at the European Marine Energy Centre (EMEC) in Orkney in September 2010. However, it was later replaced with a 1 MW turbine in January 2013. The blade's span is 5.25 m in length, with a weight of 1588.59 kg. Through several modal tests, its natural frequency was determined to be approximately 18 Hz. The blade profile is defined by the NACA 63-4XX aerofoil series, featuring a circular root. As shown in Figure 1b, the root is constructed using an iron cast to accommodate bolt holes needed for securing the blade to the rotor hub. Comprising various components, the blade includes a skin, ribs, two shear webs, and thick spar caps. The thickness-to-chord ratio of the blade varies, decreasing from 55% at the root to a minimum of 18% at the tip.

The blade skin is crafted from an 8 mm glass fibre ±45° unidirectional prepreg. The spar, depicted in red in Figure 1b, is formed from carbon fibre unidirectional prepreg. As for the shear webs, they are composed of a cross-ply carbon fibre prepreg. The ribs, situated perpendicular to the spar, are spaced at 300 mm intervals throughout the blade. These ribs have an "I" section design, with the web and flanges made of 3 mm and 2 mm thick cross-ply glass fibre prepreg. Lastly, a cross-ply glass fibre rear spar is positioned 100 mm away from the trailing edge, to minimise peel stresses at the skin joint during operation[9].

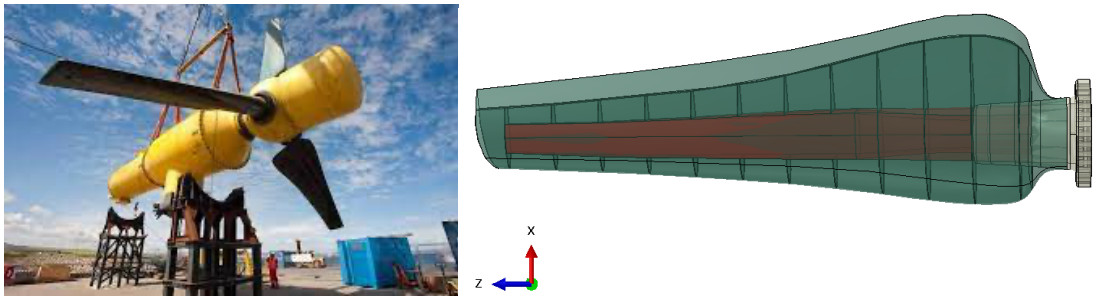

Figure 1. (a) DeepGen IV tidal turbine prior to first deployment[9], (b) CAD model.

2.2 FastBlade Testing Facility and Setup

Experimental data was collected at FastBlade, a cutting-edge research facility located at the University of Edinburgh. Specifically designed to evaluate large and slender structures ranging from 2 to 14 meters in length, this facility can subject these structures to both static and fatigue loads. With its novel regenerative system, accelerated testing at frequencies of up to 1 Hz is possible, and a maximum load capacity of 1 MN.

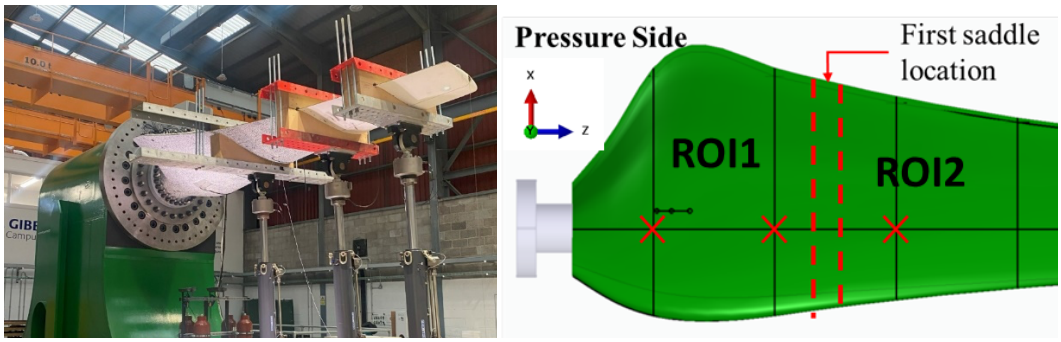

Figure 2. (a) Experimental setup with three saddles clamped to the blade. (b) Main rosette strain gauge locations cross marked and regions of interest (ROI) for DIC.

The experimental setup, as depicted in Figure 2a, involves the blade described in Section 2.1 onto the test rig. The blade is oriented with the pressure side facing downward and the suction side facing upward. Three actuators are positioned at 2.27 m, 3.56 m, and 4.58 m from the root. In the first test, three M24 steel rods on each side of the saddle were used to apply the clamping force with a torque wrench. For the second test, a single M36 steel rod on each side of the saddle was tensioned using a hydraulic bolt tensioner. The testing procedure involved a static test at 100% of the design load. Each of the three actuators applied a load of 95 kN, which was gradually ramped up from zero, followed by a holding phase at the peak load, and finally, a ramp-down phase. Each phase lasted 60 s. Subsequently, a fatigue load was introduced, operating at 0.5 Hz for 30 cycles.

2.3 Instrumentation

2.3.1 Sensors

A total of 117 channels were used to log data, comprising load cells, accelerometers, extensometers, thermocouples, potentiometers, as well as linear and rosette strain gauges. The linear and rosette strain gauges have a strain limit of 5% and 3%, respectively. Figure 2b illustrates the placement of the most relevant rosette strain gauges along the blade.

They are positioned at one-meter intervals from the root to the area beyond the first saddle, with three locations on the pressure side and one on the suction side. The first three strain gauges are situated along the x-axis at the trailing edge, centreline, and leading edge, respectively. The fourth strain gauge is located at the centreline on the suction side.

2.3.2 DIC Setup

The DIC images were acquired and processed using the MatchID software[10], captured by a setup of six cameras operating in pairs. These cameras' specific characteristics are detailed in Table 2. Each set of cameras had a different target: the first set captured images near the blade's root, the second set targeted the region close to the first saddle, and the third set covered all surfaces between the first and second saddles. Given that all sets operated in a stereo configuration, calibration was crucial to establish correlation between the pairs. For calibration purposes, approximately 150 high-resolution images were taken of a calibration plate featuring 107 dots evenly spaced by 50 mm. Each set of cameras underwent individual calibration, and the average error across all sets was 0.03 pixels.

Subsequently, the exposure settings of the cameras ranged from 11 to 13 ms, depending on the prevailing lighting conditions during the test. During the clamping phase of the test, the DIC cameras captured images at a rate of 2 Hz. The image capture rate was reduced to 1 Hz during the static phase and increased to 5 Hz for the fatigue phase of the test. To facilitate the DIC processing, the pressure side of the blade was covered with 6mm speckles, and four fiducials were placed to establish a frame of reference.

Table 2. FLIR Blackfly S USB3 (BFS-U3-88S6M-C) camera specifications[11].

Resolution	Framerate	Megapixel	Chroma	Sensor	Pixel size	ADC
4096x2160	32	8.9	Mono	SonyIMX267	3.45	12-bit

2.3.3 Preload Equipment

In the initial test, the clamping force was applied using a torque wrench, which had five evenly spaced steps ranging from 27.1 Nm to 81.4 Nm. The process involved tightening the three M24 bolts on one side of the saddle first, then moving to the other side of the saddle before increasing the step on the applied torque. For the subsequent test, a bolt tensioner, specifically the HTS20 M36 tensioner manufactured by Tension Pro, was used. This tensioner boasts a maximum pressure of 1,500 bar, a maximum load of 443 kN, a hydraulic pressure area of 2.954 mm^2, and a maximum stroke of 15 mm[12]. Two of these bolt tensioners were employed simultaneously, with one placed on each side of the saddle. As a result, the previous six M24 steel rods were replaced by two M36 steel rods. The hydraulic pressure was first ramped up to 300 bar and then reduced to 150 bar.

2.4 Methodology

2.4.1 Preload and Loading Conditions

The primary objective of a clamped saddle system is to ensure sufficient stability during a test, preventing the blade or the MDF from failing in compression or slipping. However, existing literature lacks information on how to calculate the necessary clamping force for securing the saddles. Current practices typically involve estimating the preload based on the target load at each saddle, without considering factors such as the blade geometry, mechanical properties, or bolt characteristics. To address this issue, several approaches

can be adopted for the saddle-blade system by using a bolted joint design methodology. The most simplified calculation assumes that the preload should reach the maximum value before the clamping force poses a risk of damaging the blade or the MDF. In this case, the main limiting factor is the yield strength of the bolt, expressed in Equation 1:

$$F_{PL} = LF \cdot \sigma_y \cdot A_t \quad (1)$$

Where *LF* is a load factor between 0.7 and 0.9, σ_y is the yield strength of the bolt, and A_t is the tensile stress area of the bolt, which considers the area reduction caused by the threads. As torque wrenches are the most used tools to achieve a predetermined preload, Equation 2 is often used to estimate the torque required to meet the preload force calculated in Equation 1:

$$T_{PL} = \left[\left(\frac{d_m}{2D}\right)\left(\frac{\tan\lambda + f\sec\alpha}{1 - f\tan\lambda\sec\alpha}\right) + 0.625\, f_c\right] \cdot F_{PL} \cdot D \quad (2)$$

Where T_{PL} is the applied torque, d_m is the average of the major and minor diameters, D is the nominal bolt diameter, λ is the lead angle of the thread, f is the coefficient of thread friction, α is the thread angle, and f_c is the coefficient of collar friction. The term inside the brackets is often referred as the nut factor K_n which typically has a value of 0.2 but varies depending on the application[13]. The existence of friction and shear between the joint parts and the bolt can reduce the accuracy of this approach by as much as 25%.

The most precise approach to determining the preload is by measuring the elongation of the bolt as the preload is applied. However, implementing this method in the current experiment conditions requires more robust equipment, such as ultrasonic displacement sensors or bolt tensioners. Bolt tensioners are specialised tools capable of achieving accurate and controlled bolt tension. They operate by applying hydraulic pressure to extend the bolt, resulting in a specific preload. Typically, a bolt tensioner consists of a hydraulic cylinder, piston, and a reaction device that engages with the threaded end of the bolt and the nut. By applying a pure tensile load, factors like friction, shear, and lubrication are eliminated, reducing uncertainty and variability. Each tensioner manufacturer provides a relationship between the total hydraulic pressure applied and the desired bolt preload, as described in Equation 3:

$$P_h = \frac{F_{PL}}{A_h} \cdot \left(1.01 + \frac{D}{G}\right) \quad (3)$$

Where P_h is the hydraulic pressure for a desired bolt preload, A_h is the hydraulic pressure area, and G is the bolt grip length. The term in brackets is called the load transfer allowance and can be replaced by a factor which must be determined experimentally for more accurate results. As the desired bolt preload is unknown for this experiment, Equation 3 will be solved for F_{PL} by testing a range of hydraulic pressures.

2.4.2 Digital Image Correlation (DIC)

DIC, an optical technique, offers non-intrusive means of measuring deformation on the outer surface of a structure. It has demonstrated accurate results in full-scale wind turbine blade assessments[14] and is currently used as a validation tool in tidal blade tests. Through

tracking pixel movement in camera images, DIC enables the interpolation and generation of a comprehensive deformation field. To achieve precise displacement measurements on a flat specimen, the image is divided into subsets of pixels, and correlation functions like the zero mean normalized sum of squared differences (ZNSSD) in Equation 4 are employed to identify unique subsets in the deformed images:

$$C(I, I^*, u_1, v_1, u_2, v_2, n) = \frac{\frac{1}{(2n+1)^2}\sum_{i,j=-n}^{n}\prod_{t=1}^{2}\left(I_t(u_t+i, v_t+j) - \bar{I}(u_t, v_t, n)\right)}{\sigma(u_1, v_1, n)\cdot\sigma^*(u_2, v_2, n)} \quad \text{.....(4)}$$

Where u, v represents the pixel coordinates, while n denotes the subset size. The variables σ and σ^* refer to the standard deviations, and I and I^* represent the images captured before and after the motion. A correlation function, C, close to one indicates that the subset has been successfully identified in the deformed image. However, in real-world scenarios, images often contain noise originating from various sources, making the zero mean normalized sum of squared differences (ZNSSD) function advantageous as it accounts for light variation noise. Nonetheless, the correlation function may never achieve a perfect match, encouraging the use of interpolation and shape distortion techniques.

3. Results and Discussion

3.1 Mechanical Torque Wrench Analysis

Due to safety concerns regarding manual manipulation near the blade when using the torque wrench method, it was not feasible to conduct both static and fatigue tests. Consequently, the data collected for this experiment solely pertains to the clamping phase, acquired from the sensors and DIC images. For this test, the initial conditions were set after typical static and fatigue tests, during which the saddles were already clamped to the blade. Subsequently, the bolts of the first saddle were gradually loosened until a 1 mm gap became visible between the saddle and the blade, as illustrated in Figure 3a for the first 20 min. During this loosening process, the strain on the pressure side of the blade decreased, resulting in a strain reduction of 115 με at 2 m from the root. Following this, the bolts were tightened again, reaching the maximum allowable value specified by the torque wrench, which is 81.4 Nm.

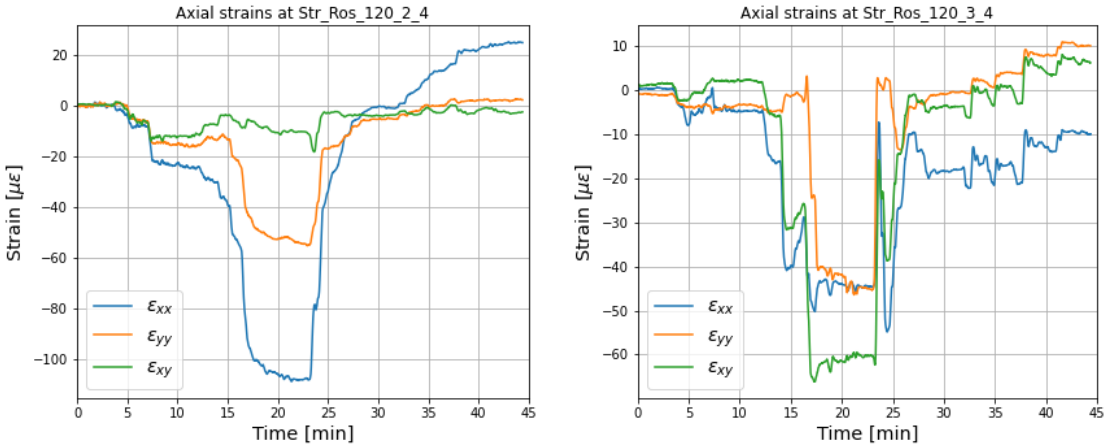

Figure 3. Axial strains at: (a) 2 m from the root, (b) 3 m from the root, in the pressure side of the blade and parallel to the global z-direction.

The strain magnitudes on the suction side of the blade are notably lower compared to the pressure side, as evident in Figure 4. At 2 m from the root, the maximum absolute principal strain measures approximately 115 με on the pressure side and only 12.5 με on the suction side. This disparity indicates that the disturbance varies based on the part of the saddle that can move freely in one of the translational degrees of freedom. Overall, the data presented in Figure 3 and Figure 4 reveals that the final strain readings do not align with the initial balanced strain. This discrepancy may be attributed to the clamping force gradually decreasing over time. As a system comprising multiple components, this reduction could result from factors such as embedment, a creep effect on the MDF or the steel frame, or a combination of these influences.

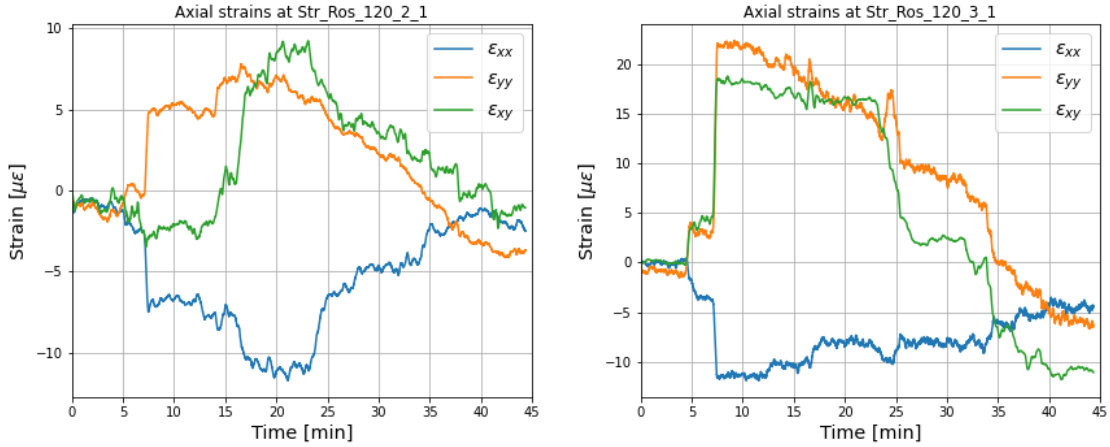

Figure 4. Axial strains at: (a) 2 m from the root, (b) 3 m from the root, in the suction side of the blade and parallel to the global z-direction.

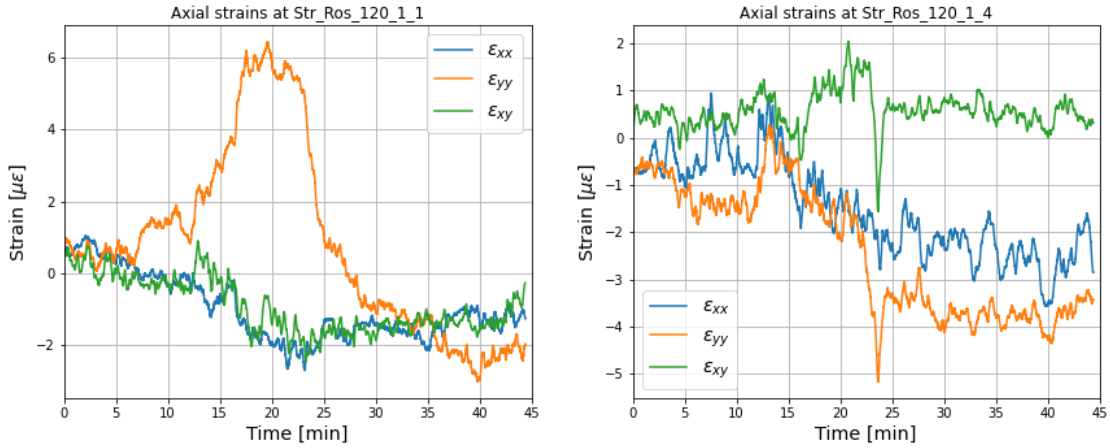

Figure 5. Axial strains at the centreline and 1 m from the root: (a) in the suction side, (b) in the pressure side of the blade.

When examining the strains at 1 m from the root, the impact of the saddle is further minimised, as demonstrated in Figure 5. The maximum absolute principal strain values are 6.5 με for the pressure side and 5.3 με for the suction side. These magnitudes can be regarded as negligible since they account for less than 1% of the strain values recorded during static and fatigue tests. Using Equation 2, and assuming a nut factor of 0.2, it is estimated that each bolt experiences a clamping force of approximately 17 kN. Notably, there were no indications of slipping observed during previous tests, even with a similar

clamping force applied. By applying Equation 2, the total clamping force is estimated to be 102 kN, which is 1.08 times the desired load from each actuator during a static test.

3.2 Hydraulic Bolt Tensioner Analysis

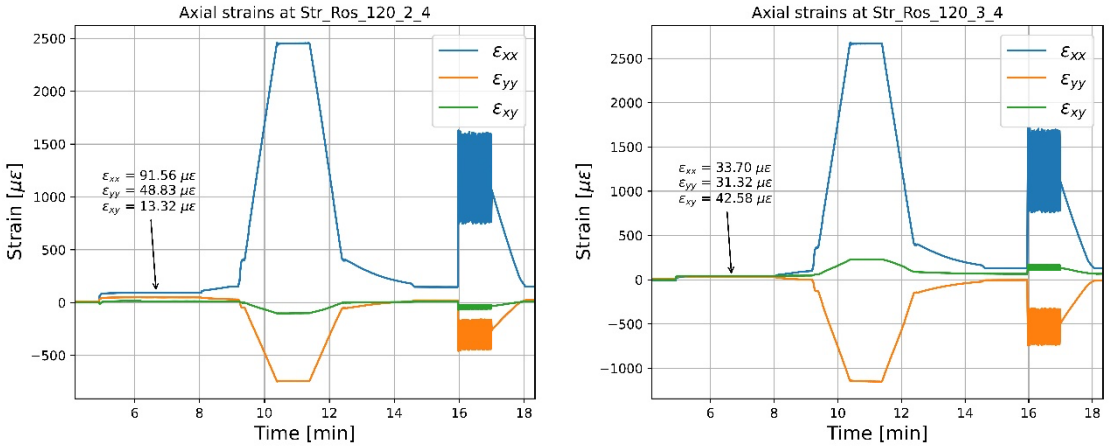

Figure 6. Axial strains at: (a) 2 m from the root, (b) 3 m from the root, at the centreline in the pressure side of the blade, during all three phases of the test.

The bolt tensioners were positioned at the upper saddle on both sides of the steel frame and connected to a single pump for hydraulic pressure control. The hydraulic pressure was initially set to 150 bar for the first phase of the experiment, followed by a static phase and a fatigue test at 0.5 Hz. Figure 6 displays the axial strain measurements from all three phases of the experiment, taken at various locations on the pressure side of the blade. The clamping force was maintained for 200 s, with the static phase commencing at 9 min and the fatigue phase beginning 16 min after the start of the test. Throughout this test, the maximum principal strain value recorded was 2,585 με at 3 m from the root on the pressure side of the blade. Comparing this with the maximum value during the clamping phase, which is approximately 60 με, it amounts to 2.2% of the total load. For strains located at 2 m from the root, the contribution from the clamping phase increases to 4%.

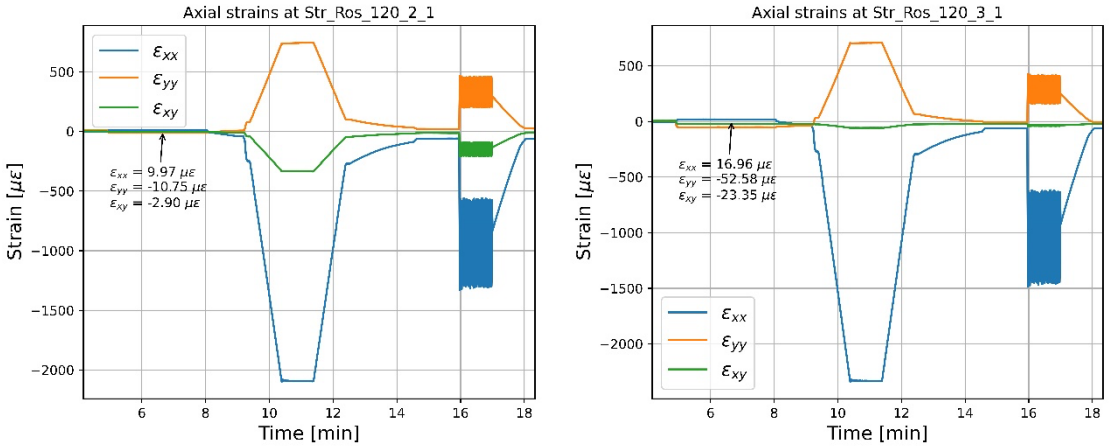

Figure 7. Axial strains at: (a) 2 m from the root, (b) 3 m from the root, at the centreline in the suction side of the blade, during all three phases of the test.

Figure 7 illustrates the strain gauge analysis on the suction side of the blade. There is an increase in maximum strain of 1.7% at 2 m and 2.6% at 3 m from the root. This contribution increases when comparing the clamping and fatigue phases. At 2 and 3 m from the root, the troughs for the maximum principal strains measure approximately 120 με and 79 με, respectively. The effect of the clamping force adds an additional 9.84% and 27.42% to these strains on the composite blade. The strain gauge data were correlated with the DIC processing results, as depicted in Figure 8. After applying a hydraulic pressure of 150 bar to both M36 bolts, the out-of-plane displacement, *W*, is observed. As expected, the area between the two shear webs sinks, leading to a protrusion on the skin between the right shear web and the rear spar. However, the existence of a rib (indicated by the red dashed line in Figure 8) at the root hinders the propagation of this out-of-plane displacement. Therefore, it can be inferred that ribs or any skin support structure inside the blade play a significant role in constraining the disturbed area caused by the saddle.

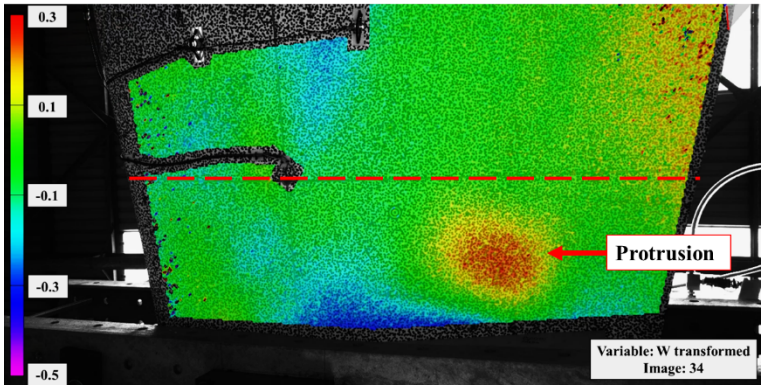

Figure 8. Out-of-plane deformation in ROI 1 after a 150-bar hydraulic pressure applied to the bolts, in mm.

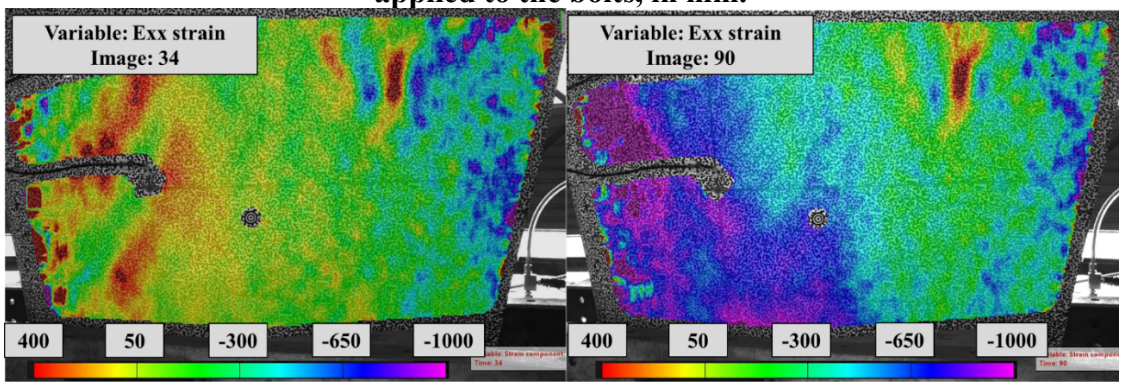

Figure 9. Longitudinal strain in με: (a) during the clamping phase, (b) during the static loading, based on the DIC images from ROI 1.

The strain field computation involved quadratic interpolation and the Euler-Almansi strain calculation, with a window tolerance of 50% and a virtual strain gauge (VSG) size of 15x15 pixels. These parameter settings ensured that the strain field matched the readings obtained from the strain gauges located in the same region, as demonstrated in Figure 9. Consistent with the findings in the out-of-field deformation field, the presence of the rib maintained similar strain values during both the clamping phase and the static loading in the area distant from the saddle system. Any increase in strain values was confined to a region within half a chord length from the fixture. A distinct strain behaviour was observed at ROI 2 when examined using the third set of cameras, as presented in

Figure 11. The interaction of the second saddle with this particular region led to an overlapping of the clamping forces from both fixtures. The presence of a rib located between the two saddles effectively split the disturbed area caused by the load introduction points located at each side of ROI 2.

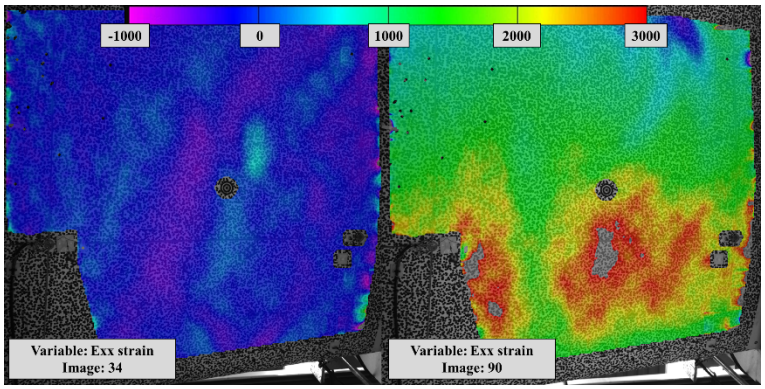

Figure 10. Longitudinal strain in με: (a) during the clamping phase, (b) during the static loading, based on the DIC images from ROI 2.

4. Conclusions

Tidal stream turbines face the significant challenge of becoming the primary source of power generation from tidal kinetic energy, and their performance heavily relies on the quality and reliability of the composite blades used. Common load introduction methods, like saddle systems, are employed for composite blade testing. However, existing standards and guidelines lack detailed specifications or practices to mitigate undesired effects during testing. Hence, this research aimed to analyse and minimise the induced effects in full-scale composite tidal turbine blades by investigating the areas surrounding the load introduction points. This investigation is carried out using strain gauge measurements and digital image correlation (DIC) techniques. The experimental data for this study was gathered at FastBlade, the world's first full-scale regenerative fatigue test facility for composite tidal turbine blades. The blade specimen used in the experiment is from the DeepGen IV tidal project, comprising cast iron, carbon, and glass fibre composites. The research quantifies the clamping force required to fix the saddles and estimates it based on factors like the target load at each saddle, blade geometry, mechanical properties, bolt characteristics, and the bolt tightening mechanism. Two clamping mechanisms were tested: the torque wrench method and the hydraulic bolt tensioner. The torque wrench method resulted in a total estimated clamping force of 102 kN or 1.08 times the design load from the actuator. Under these conditions, no slipping was observed, and the strain values at one chord length away from the saddle were negligible, representing less than 1% of the strain values during static and fatigue loading. On the other hand, the use of hydraulic bolt tensioners provided a more accurate clamping force measurement. During the experiment, a hydraulic pressure of 150 bar was applied on both saddle bolts before running static and fatigue tests. The findings revealed a maximum strain contribution from the clamping force of 27.42% at the closest strain gauge from the saddle during fatigue testing, indicating that low-cycle fatigue tests can be compromised if these induced effects are not considered. Furthermore, the analysis of out-of-plane deformation and strain field calculations from DIC images matched and confirmed the readings from the strain gauges. The resulting strain map showed that the

increase in strain could be constrained to less than half a chord length from the fixture due to the presence of a transverse rib. Future investigations might include testing at lower hydraulic pressures and applied torques to explore the effects without compromising the integrity of the testing equipment.

Acknowledgements
First author: This research was supported by the CDT Wind & Marine Energy Systems & Structures CDT under the Engineering and Physical Sciences Research Council grant agreement EP/S023801/1.
Last author: This project has received funding from the European Union's Horizon 2020 research 466 and innovation programme under the Marie Skłodowska-Curie grant agreement No 801215 and 467 the University of Edinburgh Data-Driven Innovation programme, part of the Edinburgh and South 468 East Scotland City Region Deal.

References

1. R Burrows, N C Yates, T S Hedges, M Li, J G Zhou, D Y Chen, I A Walkington, J Wolf, J Holt, and R Proctor, 'Tidal energy potential in UK waters', Proceedings of the Institution of Civil Engineers: Maritime Engineering, Vol 162, No 4, pp 155–164, December 2009.
2. IEA, 'Renewables - Fuels & Technologies', Renewables Information 2022, 2022.
3. S A Lopez Dubon, C R Vogel, D García Cava, F Cuthill, E D McCarthy, and C M Ó Bradaigh, 'Fastblade: A Technological Facility for Full-Scale Tidal Blade Fatigue Testing', SSRN Electronic Journal, 2023.
4. P Malhotra, R W Hyers, J F Manwell, and J G McGowan, 'A review and design study of blade testing systems for utility-scale wind turbines', Renewable and Sustainable Energy Reviews, Vol 16, No 1, pp 284–292, January 2012.
5. S C Yeniceli, 'Design optimization of whiffletree systems for wind turbine blade testing', 2014.
6. D Melcher, M Bätge, and S Neßlinger, 'A novel rotor blade fatigue test setup with elliptical biaxial resonant excitation', Wind Energy Science, Vol 5, No 2, pp 675–684, May 2020.
7. E R Joergensen, K K Borum, M McGugan, C L Thomsen, F M Jensen, C P Debel, and B F Soerensen, 'Full Scale Testing of Wind Turbine Blade to Failure - Flapwise Loading', Denmark: Risø National Laboratory, 2004.
8. DNV GL, 'DNVGL-ST-0164: Tidal Turbines', 2015.
9. Huxley-Reynard C, Thake J, and Gibberd G, 'TG-RE-040-0091 Rev B Deepgen Blade Design Report', Bristol, 2008.
10. Anon, 'Metrology beyond colors | MatchID | Make metrology count', 2023.
11. Anon, 'Blackfly S USB3 | Teledyne FLIR', 2022.
12. Tension Pro, 'Standard hydraulic bolt tensioners | TensionPro', 2023.
13. Budynas Richard G J, Keith Nisbett, and Joseph Edward Shigley, 'Shigley's Mechanical Engineering Design', 9th ed. New York: McGraw-Hill, 2011.
14. B LeBlanc, C Niezrecki, P Avitabile, J Chen, and J Sherwood, 'Damage detection and full surface characterization of a wind turbine blade using three-dimensional digital image correlation', Structural Health Monitoring, Vol 12, No 5–6, pp 430–439, September 2013.